Hindawi
Geofluids
Volume 2022, Article ID 3539482, 13 pages
https://doi.org/10.1155/2022/3539482

Research Article

Pore Structure and Multifractal Characteristics of Overmature Continental Shale: A Case Study from the Xujiaweizi Fault Depression, Songliao Basin, China

Jiamin Lu,[1] Liang Yang,[1] Yingkang Zhu,[1] Lidong Sun,[1] Shuangfang Lu,[2] Pengfei Zhang,[3] Nengwu Zou,[2] and Zizhi Lin[2]

[1]*Exploration and Development Research Institute, Daqing Oilfield Corp. Ltd., Daqing, 163712 Heilongjiang, China*
[2]*Key Laboratory of Deep Oil and Gas, China University of Petroleum (East China), Qingdao, 266580 Shandong, China*
[3]*College of Earth Science and Engineering, Shandong University of Science and Technology, Qingdao, 266590 Shandong, China*

Correspondence should be addressed to Pengfei Zhang; zhangpengfei0907@sdust.edu.cn

Received 31 December 2021; Accepted 23 March 2022; Published 21 April 2022

Academic Editor: Andrea Brogi

Overmature continental shales are widely distributed in China, while few investigations have been conducted. The pore structure is a critical parameter controlling the resource potential of shale gas. However, the pore structure and heterogeneity of continental shales from the Shahezi Formation, Xujiaweizi Fault, Songliao Basin are not well revealed. In this study, helium porosity and permeability, low-temperature N_2 adsorption (NGA), mercury intrusion capillary pressure (MICP), and nuclear magnetic resonance (NMR) were applied and characterized to the pore structures of continental shales. Moreover, the heterogeneity and complexity of the pore structure were revealed by the multifractal based on the NMR T_2 spectrum. The results showed that clay minerals, quartz, and feldspar are the dominant minerals in the continental shales, and the most content of the clay minerals is the illite-smectite. The studied shales are the low porosity (mean 1.73%) and the ultralow permeability (mean 0.0707 mD) tight reservoirs. The hysteresis loops of ten shales belong to Types H2 and H3, characterized by high special surface area (mean 5.28 m^2/g) and pore volume (mean 14.15×10^{-3} cm^3/g). The pore size distributions are unimodal, and Type H3 shales have more larger pores than Type H2 shales. MICP results indicate that the pore-throats are almost less than 20 nm. NMR T_2 spectra commonly show three peeks, *i.e.*, p1 (<1 ms), p2 (1~20 ms), and p3 (>20 ms) with the small $T_{2,gm}$ values, ranging from 0.18 ms to 1.36 ms (0.69 ms), which suggests that more nanopores are in the continental shales. Moreover, the average movable fluid percentage is low, ranging from 1.22% to 15.08% (mean 6.84%). The singularity strength range ($\Delta\alpha$) shows that pore structures are heterogeneous. And the heterogeneity and complexity can be better revealed by the multifractal spectra rather than a monofractal model.

1. Introduction

Shale gas existing in free, adsorbed, and dissolved states in the organic-rich shales is considered as a future energy unconventional source [1]. The exploration and exploitation of shale gas have been made remarkable achievements in North America, called the "shale gas revolution" [2]. Recently, a series of breakthroughs have been obtained in high maturity marine shales in South China [3–7]. Meanwhile, lots of investigations have been conducted on the marine shales (such as Longmaxi, Wufeng, and Qiongzhusi Formations). However, few studies have been focused on the overmature continental shale, which is widely distributed in continental sedimentary basins in China, such as the Songliao Basin and Ordos Basin [8]. Therefore, it is necessary to reveal the characteristics of high maturity continental shale to evaluate shale gas potential.

Pore structure is one of the most critical factors for determining the volume, state, and flow of shale gas [9]. Consequently, it is essential to understand the pore structure characteristics of continental shale to evaluate continental shale gas better. Previous studies suggested that shale is a

complex and heterogeneous porous medium characterized by larger amounts of nanometer pores and plenty of clay minerals and organic matter [10–13]. Thus, lots of specialized techniques have been developed to investigate the shale pore structures. Overall, these techniques can be divided into two categories: direct methods and indirect methods [14]. The direct method is also called radiation imaging methods, including X-ray computed tomography (CT), field emission-scanning electron microscopy (FE-SEM), focused ion beam-scanning electron microscopy (FIB-SEM), and broad-ion-beam milling-scanning electron microscopy (BIB-SEM) [15–20]. Plenty of direct information, such as pore types and morphologies, can be obtained from these imaging methods. Indirect methods, *i.e.*, mercury intrusion capillary pressure (MICP), low-pressure gas (N_2 and CO_2) adsorption (GA), and nuclear magnetic resonance (NMR), can provide the quantitative pore structure parameters (i.e., porosity, permeability, specific surface area, and pore size distribution) [10, 12, 21–23].

In addition, the storage and transportation capacity of shale gas is also controlled by the heterogeneity of pore structures [15]. The fractal theory is regarded as an effective method to characterize the heterogeneity and complexity of pore-fracture networks in shale [4, 6, 23–25]. Low-temperature N_2 adsorption (NGA) method combined with the FHH model has been widely used to calculate the fractal dimensions to evaluate the heterogeneity and complexity of pore structures [4, 6, 23, 24]. However, the single fractal dimension cannot reveal all the features of the fractals with heterogeneity and singularity because it characterizes the average properties [26]. Multifractal theory can provide more information about the pore structure than the single fractal dimension, which decomposes the self-similar measures into intertwined fractal sets and divides the complex fractals into several regions, characterized by the singularity strength generalized fractal dimensions [27].

Therefore, in the present study, the pore structures of the shales from the Shahezi Formation in Xujiaweizi Fault Depression were revealed using NGA, MICP, and NMR measurements. Multifractal analysis was also adopted to characterize the heterogeneity of pore structures. These results give an insight into the pore structures of the continental shales.

2. Geological Setting

Xujiaweizi Fault located in the north of the Songliao Basin, Northeastern China, is regarded as a low-angle dummy-like depression (Figure 1). It includes four substructural stripes, such as Anda-Xingcheng Uplift Belt, Xuxi Sag Belt, Xudong Sag Belt, and Xudong Slope Belt, with an exploration area of about 5350 km^2 (Figure 1(c)). The sedimentary strata in Xujiaweizi Fault include the Lower Cretaceous Huoshiling Formation, Shahezi Formation, and Yingcheng Formation [28]. Shahezi Formation was deposited in the heyday of the Xujiaweizi Fault, with multiple sets of sedimentary facies, such as fan delta, braided river delta, and lacustrine facies. The dark shales (including mudstones) are considered the primary source rocks of the natural gas in the Xujiaweizi Fault, mainly developed in the lacustrine facies. Shahezi shales contain a high abundance of total organic carbon (TOC) content as well as types II_2 and III kerogens at the evolutionary stage of high maturity to overmature [29]. They are considered as the exploration potential zone of shale gas in the Songliao Basin.

3. Samples and Methods

3.1. Samples. In this study, 10 shale samples were collected from 5 well, as shown in Figure 1(c). Series of experiments were carried out on these samples, including total organic carbon (TOC), X-ray diffraction (XRD), rock-eval pyrolysis, porosity and permeability, low-temperature N_2 adsorption-desorption (NGA), mercury intrusion capillary pressure (MICP), and nuclear magnetic resonance (NMR). Porosity and permeability, MICP, and NMR were conducted on the core plugs, while other tests were performed on the core cuttings.

3.2. Experiments

3.2.1. Helium Porosity and Permeability. Prior to the tests, shale core plugs were dried in a vacuum oven at 110°C for 24 h to remove the residual pore water. Helium porosity and permeability were conducted on a PorePDP-200 instrument, which can test the porosity range of 0.01%~40% and permeability range of $0.00001 \times 10^{-3} - 10 \times 10^{-3}\ \mu m^2$. Porosity and permeability were tested under the confining pressure of 200 psi and 1000 psi, respectively. Porosity was measured by the helium expansion method, and permeability was calculated by the transient pressure decay method.

3.2.2. Low-Temperature N_2 Adsorption-Desorption. Low-temperature N_2 adsorption-desorption (NGA) measurements were performed on a Micromeritics ASAP 2460 specific surface area and porosity analyzer. Shale samples were sieved to obtain the particle size of 0.25-0.38 mm (40-60 much), and a split of 3~5 g particle sample was used to test. Prior to the low-temperature N_2 isotherm analysis, the particle samples were dried in a vacuum oven at 383 K for 12 h. For all samples, the N_2 adsorption-desorption isotherms were collected under the relative pressure varying from 0.01 to 0.993 at 77 K. In this study, the total pore volume (PV), specific surface area (SSA), and pore size distribution (PSD) were all obtained from the adsorption branch. PV is the single pore volume obtained at a relative pressure of 0.99. SSA was calculated by the Brunauer-Emmett-Teller (BET) method from the adsorption data under the relative pressure ranging from 0.05 and 0.35, and PSD was determined by the DFT model.

3.2.3. Mercury Injection Capillary Pressure. Mercury injection capillary pressure (MICP) tests were conducted on a micromeritics AutoPore IV 9510 porosimeter. MICP measurements were carried out on the same core plugs after helium porosity and permeability tests. In this study, the mercury injection pressure ranged up to about 200 MPa, corresponding to a pore throat size as small as approximately 7 nm.

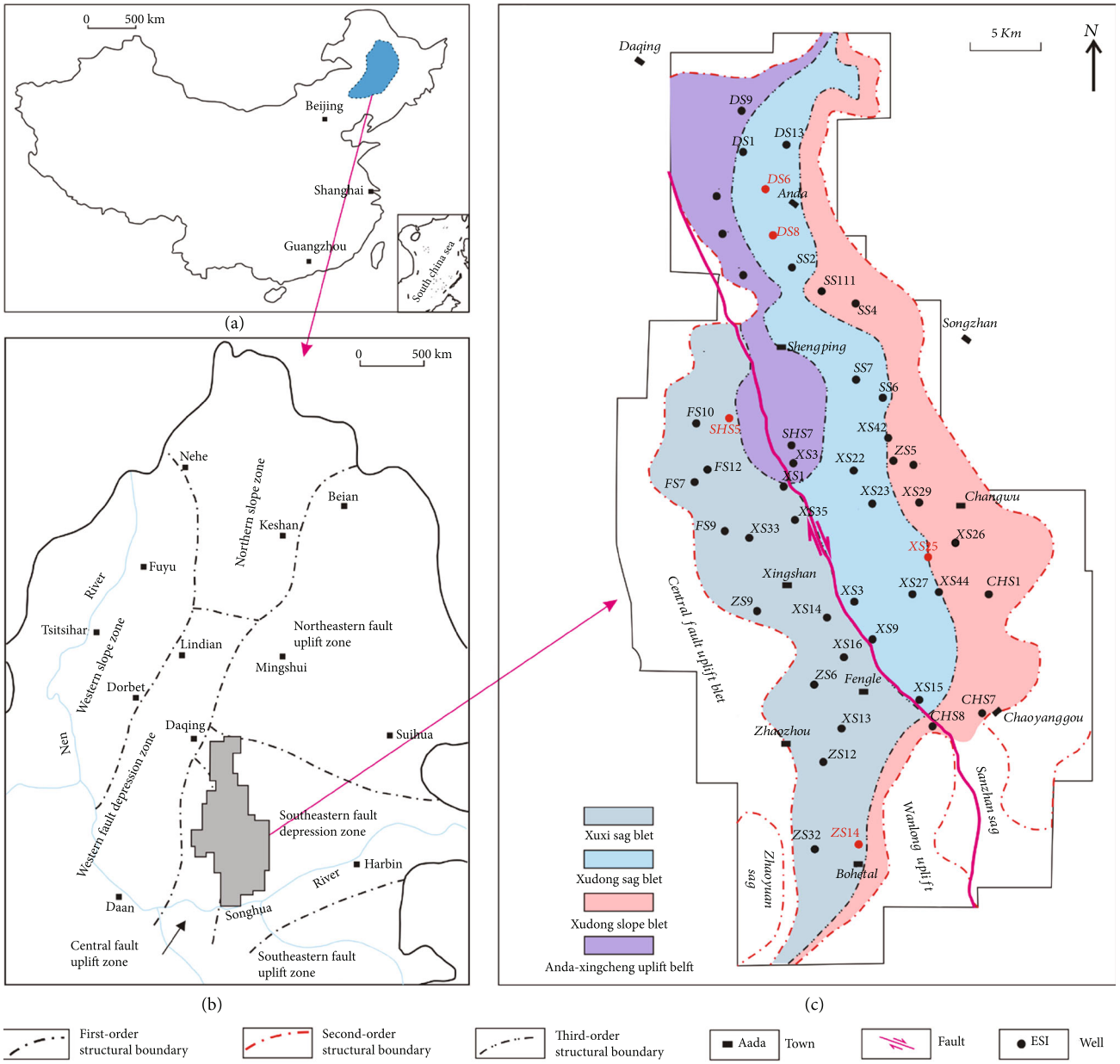

Figure 1: Geological map of Xujiaweizi Fault and sampling locations (modified from Xiao et al. [30]).

3.2.4. Nuclear Magnetic Resonance. Nuclear magnetic resonance (NMR) experiments were performed on the MesoMR23-060H-I NMR spectrometer (Suzhou, China), characterized by a relatively low magnetic field of 0.52 T and operated at 21.36 MHz. The T_2 spectrum was obtained by the CPMG spin-echo train pulse sequence with the test parameters as follows: waiting time, 3000 ms; echo number, 6000; and number of scans, 64. Moreover, the shortest echo time of 0.07 ms was used for the shale NMR tests to detect the pore as small as several nanometers [22]. The NMR experiments of dry shale samples were first conducted to reference saturated tests.

Prior to NMR measurements, shale core plugs were first dried in a vacuum oven at 110°C for 24 h. After the samples cooled to room temperature in a desiccator, the mass of the sample was first weighed by electronic balance (0.0001 g). Then, the original NMR relaxation spectra of dry samples were detected. Subsequently, the dry plugs were vacuumed for 24 h and then saturated with n-dodecane (n-C_{12}) at 10 MPa for 24 h to obtain the saturated state. After weighing, NMR measurements of n-C_{12} saturated shale plugs were conducted. Based on the mass of the dry and saturated states, the n-C_{12} wetting porosity was determined. Finally, to obtain the irreducible condition, the n-C12 saturated shale plugs were centrifuged using an MC-21 Petroleum Core Centrifuge at a centrifugal pressure difference of 2.76 MPa. Based on the dry samples' CPMG spin-echo train pulse sequences, the T_2 spectra of saturated and irreducible conditions were determined. And the NMR porosity of the samples was calculated by the saturated T_2 spectra.

3.3. Multifractal Analysis Based on T_2 Spectrum. When a low and uniform magnetic field and a short echo time are used, the T_2 relaxation time is mainly determined by the surface relaxation [10]:

$$\frac{1}{T_2} = \rho_2 \frac{S}{V}, \tag{1}$$

where T_2 is the transverse relaxation time, ms; ρ_2 is the transverse surface relaxivity, μm/s; and S/V is the surface area to volume ratio of pores, nm^{-1}. Based on Equation (1), T_2 spectrum of the saturated sample can be transformed into pore size distribution, which is the basis for studying the multifractal characteristics using NMR T_2 spectrum.

In this study, the multifractal was defined based on the generalized dimension. The process of multifractal calculation is as follows.

It was assumed that the T_2 spectrum could be segmented in N_T partitions with scale r ($r = \mathrm{O} \times 2^{-\mathrm{k}}$, O is the point number of T_2 spectrum and $2^{\mathrm{k}} \le O$), so that the probability of the ith partition ($P_i(r)$) can be written as Equation (2) [20, 31]:

$$P_i(r) = \frac{\varphi_i(r)}{\sum_{i=1}^{N_T} \varphi_i(r)}, \tag{2}$$

where $\varphi_i(r)$ is the NMR porosity of the ith partition. If the pores are with a multifractal property, the relationship between $P_i(r)$ and scale r can be expressed as Equation (3) [32]:

$$P_i(r) \sim r^{\alpha_i}, \tag{3}$$

where α_i indicates singularity strength, which characterizes the density in the ith box. Moreover, $N_\alpha(r)$ represents the number of boxes for $P_i(r)$ with singularity strengths between α and $d\alpha$, which is related to scale r and can be expressed by Equation (4):

$$N_\alpha(r) \propto r^{-f(\alpha)}, \tag{4}$$

where $f(\alpha)$ is called the multifractal spectrum.

For multifractal calculation, the partition function ($N(q, r)$) of q with scale r can be defined by Equation (5):

$$N(q, r) = \sum_{i=1}^{N_T} P_i^q(r) \propto r^{\tau(q)}, \tag{5}$$

where $\tau(q)$ denotes the mass exponent and can be written as follows:

$$\tau(q) = -\lim_{r \longrightarrow 0} \frac{\log \sum_{i=1}^{N_T} P_i^q(q)}{\log r}. \tag{6}$$

The generalized dimension D_q can be expressed as Equation (7), based on the $P_i(r)$ and q [32].

$$D_q = \begin{cases} \dfrac{1}{q-1} \lim\limits_{r \longrightarrow 0} \dfrac{\log \sum_{i=1}^{N_T} P_i^q(r)}{\log r} = \dfrac{\tau(q)}{q-1}, & q \neq 1, \\ \lim\limits_{r \longrightarrow 0} \dfrac{\sum_{i=1}^{N_T} P_i(r) \ln P_i(r)}{\ln r}, & q = 1, \end{cases} \tag{7}$$

where D_q indicates the overall singularity of each box and is strictly monotonically decreasing with increasing q. Then, according to the Legendre transformation from the q and $\tau(q)$, $f(\alpha)$ and α can be determined by Equations (8) and (9), respectively [33].

$$f(\alpha) = \alpha q - \tau(q), \tag{8}$$

$$\alpha = \frac{d\tau(q)}{dq}, \tag{9}$$

$q - D_q$ and $\alpha - f(\alpha)$ are the basic mathematical tools for describing pore structure heterogeneity and complexity.

Table 1: Geochemical characteristics of shale samples.

Sample	Depth/m	TOC/%	T_{max}/°C	S_1+S_2/mg/g
DS6-6	3543.04	2.07	517	0.5741
DS6-17	3842.46	0.33	533	0.1787
DS28-11	3022.63	1.44	508	0.7017
DS28-15	3024.78	0.81	503	0.8466
ShS5-16	3880.15	1.09	533	0.2373
XS25-2	4218.54	0.42	533	0.1859
XS25-5	4269.37	1.93	533	0.3225
XS25-6	4270.27	1.17	533	0.2323
XS25-12	4274.87	3.48	533	0.2805
ZS14-5	4032.40	1.67	533	0.2009

4. Results and Discussion

4.1. Geochemical and Mineralogical Characteristics. TOC contents, S_1+S_2 and T_{max} results of the shale samples, are listed in Table 1. The TOC content ranges from 0.33% to 3.48%, with an average of 1.44%. The values of S_1+S_2 vary from 0.1787 mg/g to 0.8466 mg/g, with a mean of 0.3761 mg/g, and the mean of the T_{max} is 526°C, with a range of 503°C-533°C, which suggests that the organic matter maturity is high maturity. As listed in Table 2, the dominant minerals in the continental shales are clay minerals, quartz, and feldspar. The clay mineral varies from 40.21% to 58.69%, with an average of 50.54%, and the quartz is between 28.35% and 58.89%, with a mean of 36.99%. The average value of feldspar is 11.52% with a range of 0%~19.29%. Moreover, the studied shales contain small amounts of calcite and orthoclase, with average 0.22% and 0.28%, respectively. As shown in Figure 2(a), three components of clay, felsic, and calcium minerals may not be appropriate to describe the mineral composition of the studied shales. Therefore, three components

Table 2: Mineral compositions of shale samples.

Sample	Brittle mineral/%					Clay mineral/%					
	Q	O	F	C	Total	I	I/S	K	Ch	S%	Cl
DS6-6	39.17	0.00	9.20	0.00	48.36	36.74	56.12	0.00	7.13	14.54	51.14
DS6-17	34.59	0.00	19.29	1.25	53.88	40.10	51.38	0.00	8.52	10.71	44.87
DS28-11	39.38	0.00	14.02	0.00	53.41	14.81	71.11	2.45	11.63	23.32	46.59
DS28-15	28.35	0.00	17.95	0.00	46.30	10.15	78.15	2.27	9.44	31.18	53.37
ShS5-16	31.28	2.79	17.28	0.00	51.34	37.00	56.61	0.00	6.39	11.49	48.66
XS25-2	58.89	0.00	0.00	0.91	59.79	24.39	68.05	1.11	6.45	17.25	40.21
XS25-5	31.50	0.00	10.67	0.00	42.17	23.06	71.88	0.00	5.06	16.52	57.83
XS25-6	39.92	0.00	7.70	0.00	40.62	16.57	80.90	0.00	2.53	21.27	58.69
XS25-12	34.58	0.00	11.29	0.00	45.87	24.69	68.54	0.00	6.78	15.53	54.13
ZS14-5	32.19	0.00	7.83	0.00	40.02	65.18	24.17	0.00	10.65	15.53	49.91

Q, O, F, and C are the quartz, orthoclase, feldspar, and calcite, respectively; I, I/S, K, Ch, and CL are the illite, illite-smectite, kaolinite, chlorite, and clay mineral, respectively.

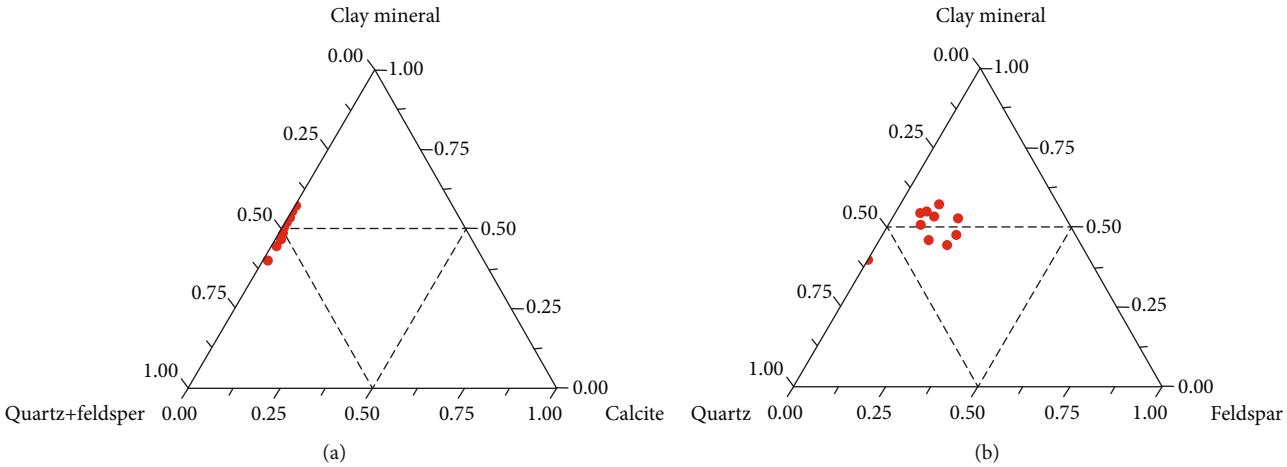

Figure 2: Shale sample mineralogical composition ternary diagram.

of clay mineral, quartz, and feldspar are more applicable, as shown in Figure 2(b). The brittle mineral ranges from 40.02% to 59.79%, with a mean of 48.18%, which means that it is accessible from the fractures in hydraulic fracturing. The most content of the clay mineral is the illite-smectite with an average of 62.69% (24.17%~80.90%), followed by illite (mean 26.27%), chlorite (mean 7.46%), and kaolinite (0.58%) (Table 2).

4.2. Porosity and Permeability. The Helium, NMR, and $n\text{-}C_{12}$ porosities of the shale samples are listed in Table 3. The helium porosity is more minor than NMR and $n\text{-}C_{12}$ porosity (Figure 3(a)) with the range of 0.35%~4.07% (mean 1.37%). And the NMR porosity varies from 0.43% to 5.47%, with an average of 2.62%, which has an excellent correlation with $n\text{-}C_{12}$ porosity (mean 2.60%, ranging from 0.35% to 5.47%), characterized by a high correlation coefficient of 0.9925% (Figure 3(a)). Moreover, the helium permeability is between 0.0003 mD and 0.2553 mD (mean 0.0707 mD). However, there is no correlation between helium porosity and permeability, as shown in Figure 3(b). NMR may be an alternative method to obtain the total porosity of shales.

Table 3: Porosity and permeability of shale samples.

Sample	Porosity/%			Permeability mD
	$n\text{-}C_{12}$	NMR	Helium	
DS6-6	2.81	2.95	0.75	0.0015
DS6-17	3.26	3.35	0.98	0.0044
DS28-11	5.24	5.25	3.15	0.0039
DS28-15	5.47	5.47	4.07	0.0049
ShS5-16	0.43	0.35	0.35	0.0003
XS25-2	1.34	1.42	0.64	0.0557
XS25-5	2.00	1.96	1.07	0.1021
XS25-6	3.25	3.45	1.26	0.1171
XS25-12	1.56	1.26	0.60	0.2553
ZS14-5	0.80	0.55	0.85	0.1614

4.3. Low-Temperature N_2 Adsorption-Desorption (NGA). According to the IUPAC classification, the nitrogen adsorption isotherms of the ten continental shales belong to Type II [34], as shown in Figure 4. The nitrogen adsorption process can be divided into three stages, i.e., low relative pressure

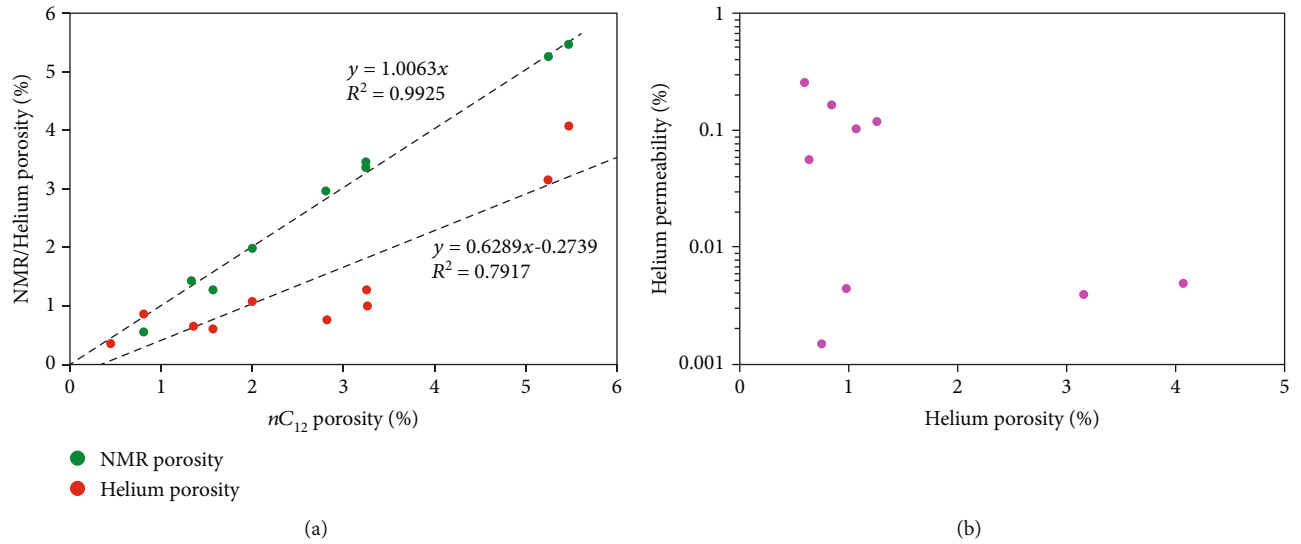

Figure 3: Porosity and permeability of shales.

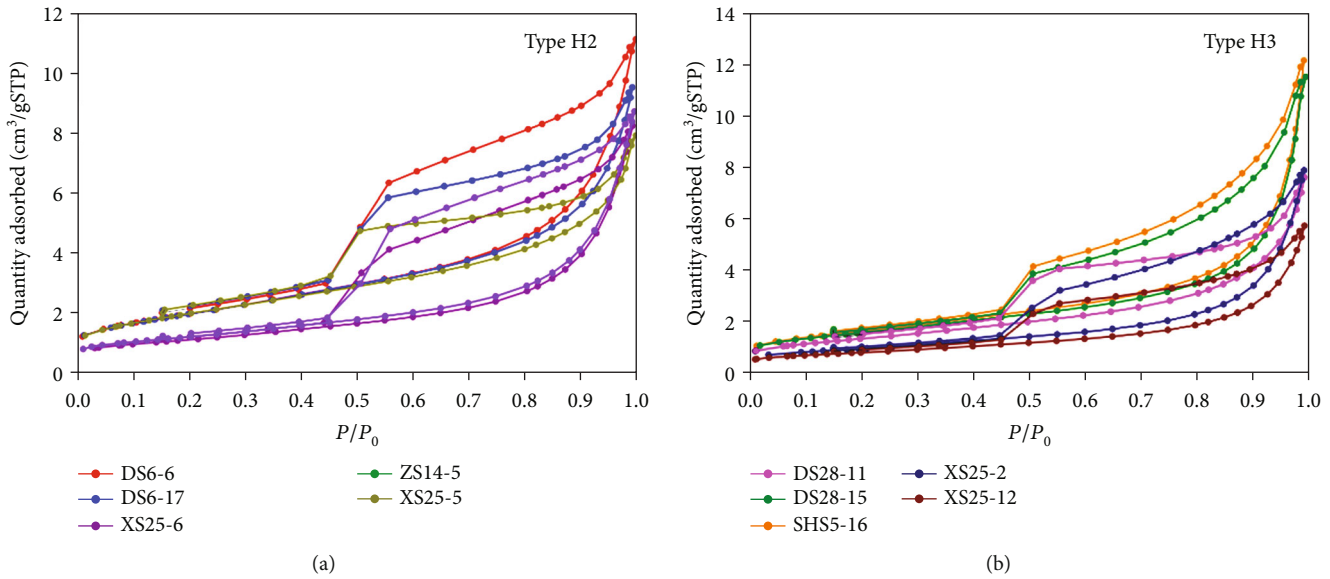

Figure 4: Nitrogen adsorption-desorption isotherms of shale samples.

Table 4: Pore structure parameters of study samples from NGA.

Sample	Loop type	BET SSA m^2/g	Pore volume 10^{-3} cm^3/g	*da* nm	Pore percentages/% <25 nm	25~100 nm	>100 nm
DS6-6		7.22	17.15	9.50	49.82	37.12	13.05
DS6-17		7.19	14.69	8.17	55.27	32.48	12.26
XS25-5	H2	4.75	15.52	13.08	40.65	45.71	13.64
XS25-6		4.03	12.72	12.63	42.25	46.62	11.14
ZS14-5		7.30	12.23	6.70	59.93	25.46	14.61
DS28-11		5.83	18.75	12.86	35.15	41.30	23.56
DS28-15		5.61	17.77	12.67	36.08	41.42	22.49
ShS5-16	H3	4.76	11.74	9.87	49.35	33.09	17.56
XS25-2		3.36	12.15	14.46	36.77	46.99	16.24
XS25-12		2.80	8.83	12.63	39.38	42.95	17.67

SSA is the special surface area; *da* is the average pore diameter.

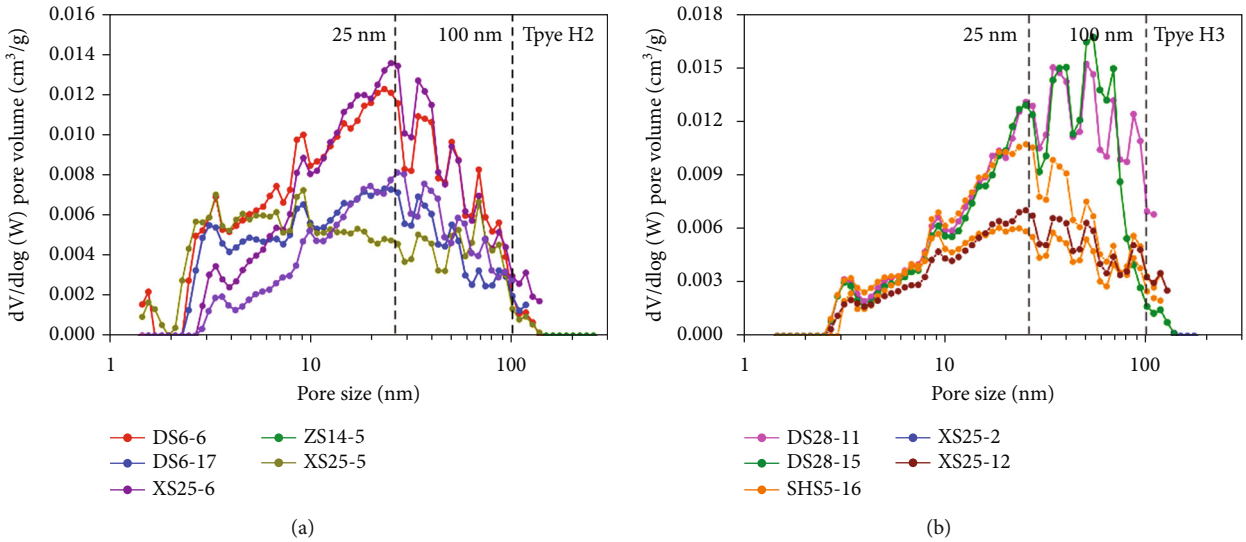

Figure 5: Pore size distributions of shales obtained from NGA by DFT model.

($p/p_o < 0.4$), medium-high pressure ($0.4 < p/p_o < 0.8$), and high pressure ($0.8 < p/p_o$), which corresponds to monolayer coverage, multilayer coverage, and capillary condensation, respectively. Moreover, a hysteresis loop appears between the adsorption and desorption branches, when the relative pressure is larger than 0.4. It indicates the dominant pore types in shales. The studied continental shales belong to two typical types: H2 and H3, based on the hysteresis loops (Figure 4 and Table 4). For Type H2, an obvious yielding point can be recognized in the desorption branch at the relative pressure of about 0.5, suggesting that the ink-bottle-shaped pores are developed. However, for Type H3, a narrow hysteresis loop appears at medium-high relative pressure and the adsorption and desorption branches are nearly parallel, indicating that the silt-shaped pores are developed.

As listed in Table 4, the SSA values of the studied shales vary from 2.80 m^2/g to 7.30 m^2/g, with a mean of 5.28 m^2/g. And Type H2 shales have higher SSA values (mean 6.10 m^2/g) than Type H3 (mean 4.47 m^2/g). The pore volume ranges from 8.83×10^{-3} cm^3/g to 18.75×10^{-3} cm^3/g, with an average of 14.15×10^{-3} cm^3/g, while Type H2 shales have similar pore volume to Types H3. Therefore, Type H2 shales are characterized by a smaller *da* (mean 10.02 nm) than Type H3 (mean 12.50 nm), which are all larger than the marine high maturity shales [4, 6]. Thus, in this study, the pore size classification of shale reservoir proposed by Zhang et al. [25] was adopted. As shown in Figure 5, the PSD of both Type H2 and H3 shales are unimodal. The peeks of Type H2 shales are located at nearly 25 nm, while the peeks of Type H3 shales are situated at the size of 25~50 nm. Thus, the pores less than 25 nm occupy the most significant proportion (mean 49.58%) of the pore volume for Type H2 shales. However, the pores between 25 nm and 100 nm make the most considerable contribution for Type H3 shales, with an average of 41.15%. Type H3 shales have larger pores than Type H2 shales, which may be more conducive to free gas.

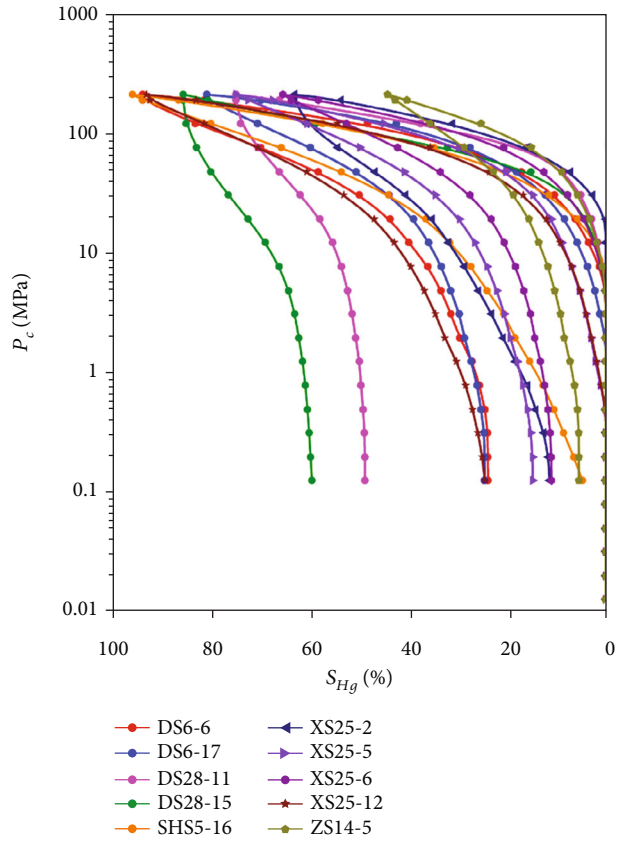

Figure 6: Mercury intrusion-extrusion curves.

4.4. Mercury Intrusion Capillary Pressure (MICP). MICP method has been widely used to characterize the pore structure of shales, and its measurement range is much larger than low-temperature N_2 adsorption-desorption method, i.e., ranging from 3 nm to 12 μm [35]. Mercury intrusion and extrusion curves of the studied shales are shown in Figure 6. It can be found that mercury began to enter into

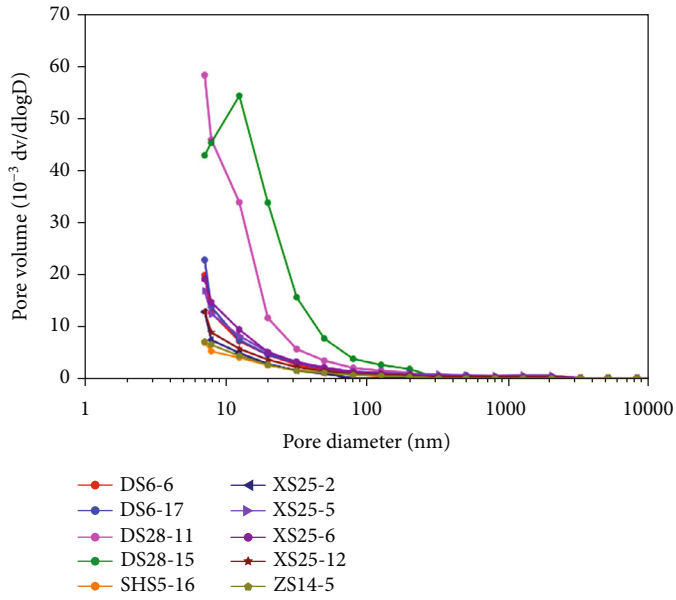

Figure 7: Pore-throat size distributions of shales obtained from MICP.

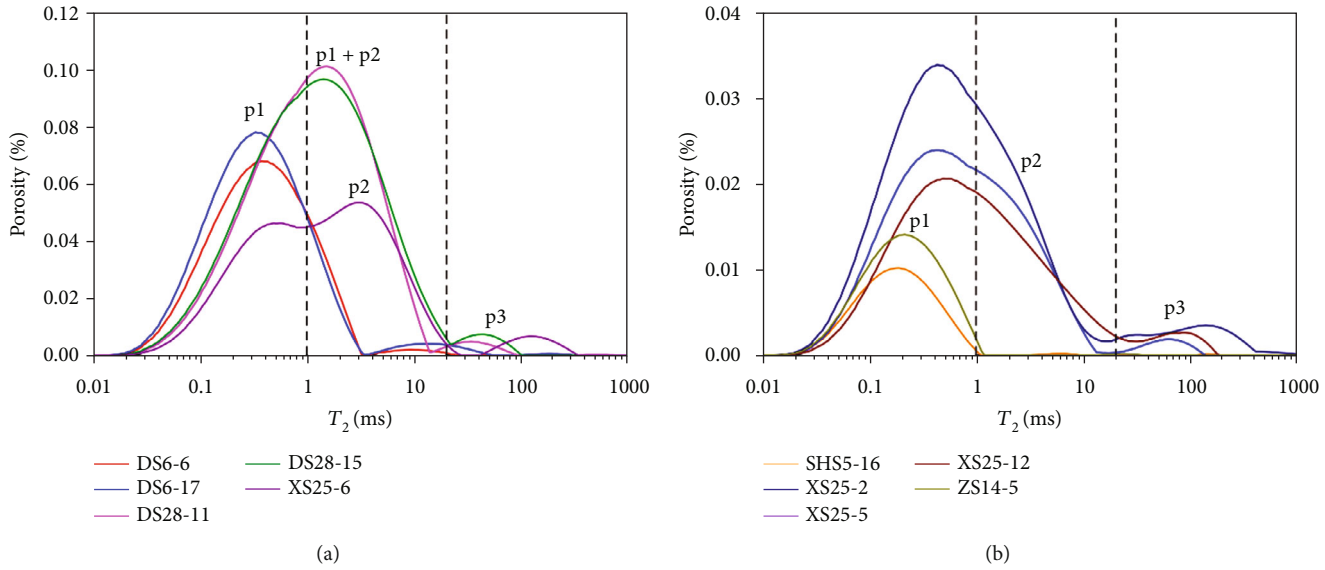

Figure 8: T_2 spectra of shale samples.

the sample, if the pressure was larger than 10 MPa. When the pressure was larger than 40 MPa, mercury quickly entered into the samples in large amounts. The pore-throat size distributions were calculated using the Washburn equation based on the mercury intrusion curves. Figure 7 shows that pore-throat sizes of the studied shales are almost less than 100 nm and the pore-throat size distributions are semimodal, except for sample DS28-15, which has a peak of about 20 nm. The mercury intrusion volume continues to increase, so there is no absolute peak when the mercury intrusion pressure reaches the maximum, resulting in a semimodal peek.

4.5. Nuclear Magnetic Resonance (NMR)

4.5.1. Pore Structure Characteristics. NMR T_2 spectra at saturated condition (S_o) of ten shale samples are shown in Figure 8, and the T_2 spectra show three peeks, *i.e.*, p1 (<1 ms), p2 (1~20 ms), and p3 (>20 ms), which is similar to the T_2 spectra of shale oil reservoirs and coals [10, 36]. However, p1, p2, and p3 cannot be identified in some samples. For example, in samples DS28-11 and DS28-15, p1 and p2 merge into a peek (p1+p2). Based on the T_2 spectra, pore structure parameters, such as $T_{2,gm}$, $T_{2,35}$, and $T_{2,50}$, can be determined. $T_{2,gm}$ is the T_2 logarithmic mean value, indicating the integrated characteristics of T_2 spectrum. $T_{2,35}$ and $T_{2,50}$ are the T_2 values corresponding to the 35% and 50% saturation on the T_2 reverse

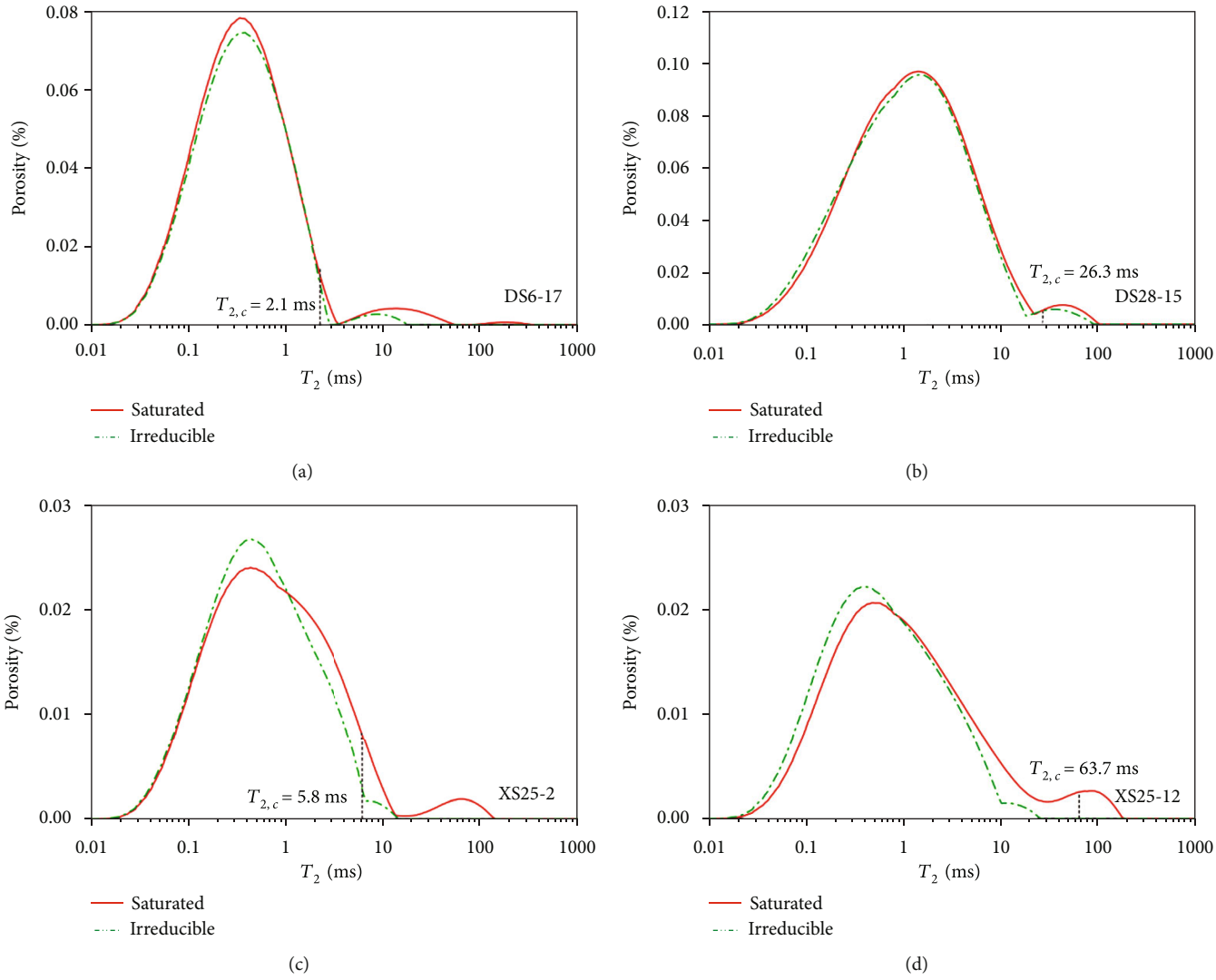

Figure 9: T_2 spectra of shales at saturated and irreducible conditions.

Table 5: Pore structure parameters obtained from NMR.

Sample	$T_{2,gm}$/ms	$T_{2,35}$/ms	$T_{2,50}$/ms	T_{2c}/ms	Movable fluid/%	Movable porosity/%
DS6-6	0.35	0.60	0.34	2.10	3.53	0.10
DS6-17	0.37	0.55	0.34	1.70	6.69	0.22
DS28-11	1.03	2.20	1.35	28.00	1.22	0.06
DS28-15	1.36	2.80	1.59	26.30	2.07	0.11
SHS15-16	0.18	0.26	0.18	0.40	14.84	0.05
XS25-2	0.54	1.06	0.47	5.80	6.13	0.09
XS25-5	0.61	1.25	0.40	3.50	15.08	0.30
XS25-6	0.98	2.03	0.77	13.10	5.99	0.21
XS25-12	0.86	1.87	0.51	63.70	2.49	0.03
ZS14-5	0.58	0.29	0.19	10.20	10.37	0.06

accumulative curve, respectively [31]. The $T_{2,gm}$ values range from 0.18 ms to 1.36 ms, with a mean of 0.69 ms, indicating more nanopores in the continental shales. The $T_{2,35}$ values vary from 0.26 ms to 2.80 ms (mean 1.29 ms), which are larger than $T_{2,gm}$, and the average of $T_{2,50}$ values is 0.61 ms (0.18~1.59 ms).

NMR T_2 spectra at irreducible condition (S_{ir}) of some shales are illustrated in Figure 9, commonly lower than those

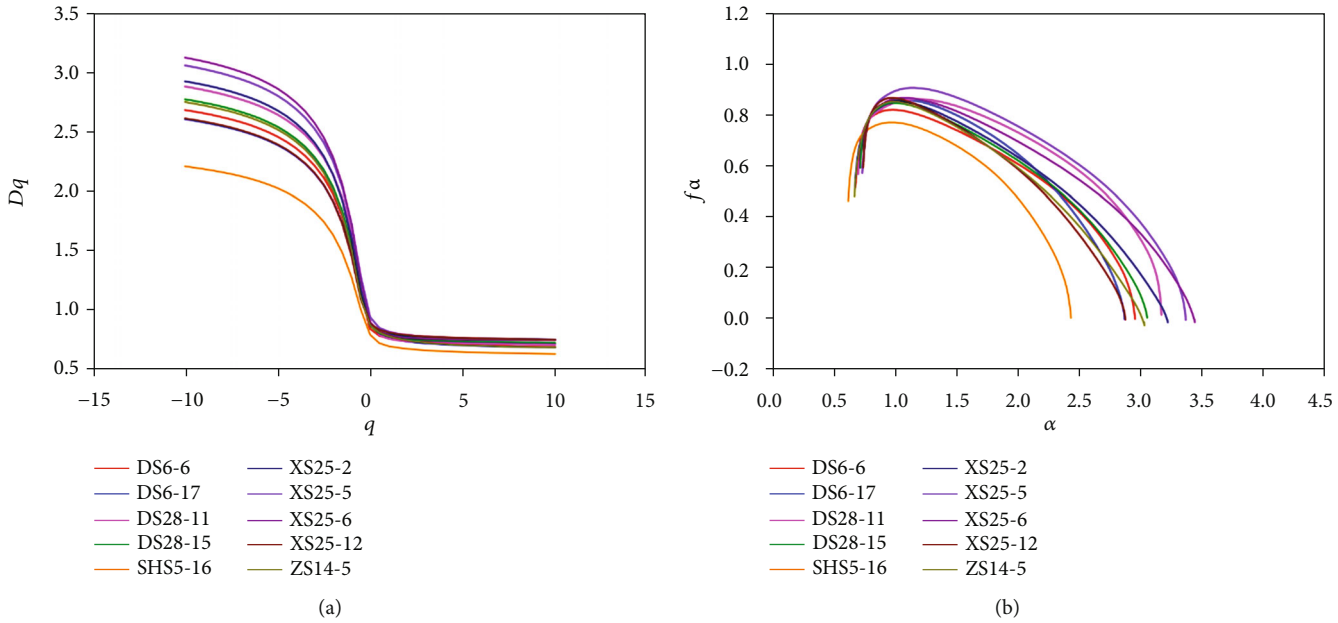

Figure 10: Generalized dimensional (a) and multifractal spectra (b) of shale samples.

Table 6: Multifractal parameters of shale samples.

Sample	D_0	D_1	D_2	D_{min}	D_{max}	α_{max}	α_{min}	$\Delta\alpha$	α_0	A
DS6-6	0.85	0.77	0.74	2.68	0.70	2.95	0.68	2.27	1.11	0.23
DS6-17	0.89	0.77	0.74	2.60	0.69	2.86	0.67	2.19	1.18	0.30
DS28-11	0.91	0.77	0.75	2.88	0.72	3.16	0.70	2.46	1.31	0.33
DS28-15	0.88	0.78	0.76	2.77	0.73	3.04	0.72	2.33	1.11	0.20
SHS15-16	0.80	0.70	0.68	2.21	0.64	2.43	0.62	1.81	1.06	0.32
XS25-2	0.89	0.80	0.79	2.92	0.76	3.21	0.74	2.47	1.14	0.19
XS25-5	0.95	0.82	0.80	3.05	0.75	3.36	0.73	2.62	1.29	0.27
XS25-6	0.90	0.80	0.77	3.12	0.75	3.43	0.74	2.68	1.23	0.22
XS25-12	0.89	0.82	0.80	2.61	0.76	2.87	0.74	2.13	1.06	0.18
ZS14-5	0.88	0.79	0.75	2.74	0.69	3.02	0.67	2.35	1.09	0.22

at S_o. Specifically, p1 at S_{ir} is similar to that at S_o, while p2 at S_{ir} is lower than that at S_o. Moreover, p3 mainly shifts toward the lower T_2 values at S_{ir}. However, it also can be found that p1 at S_{ir} is larger than that at S_o. The reason may be that fluids in the pore center were expelled during the centrifugation. In contrast, those at the pore edge were retained because of the complexity of pore morphology, leading to the increase in p1 amplitude at S_{ir}. T_2 cutoff values (T_{2c}) were calculated based on the T_2 spectra at S_o and S_{ir} and listed in Table 5. T_{2c} values are between 0.4 ms and 63.70 ms, with an average of 15.48 ms. The average movable fluid percentage is 6.84%, ranging from 1.22% to 15.08%, similar to overmature marine shales [37, 38], indicating that the pore structure is more complex. Movable porosity is the product of NMR porosity and movable fluid percentage, ranging from 0.03% to 0.30% (mean 0.12%).

4.5.2. Multifractal Characteristics. In this study, the range of q was set from -10 to 10 at 0.5 intervals. Therefore, D_{min} and D_{max} are the D_{-10} and D_{10}, respectively. Multifractal characteristics were analyzed for ten selected shale samples. The $q - D_q$ distributions of ten shales are shown in Figure 10(a), which exhibit two variation tendencies. When q is less than 0, D_q decreases rapidly with q increasing, while D_q decreases slightly as q increases when $q > 0$. This is similar to the multifractal characteristics of tight sandstones based on NMR T_2 spectra [31]. The multifractal parameters D_0, D_1, and D_2 are the capacities, information, and correlation dimensions listed in Table 6. All the samples show the same relationship, i.e., $D_0 > D_1 > D_2$, which suggests NMR T_2 spectra for all samples have multifractal nature. Moreover, D_0 is a parameter to characterize the complexity of pore structure, with the range of 0.80~0.95 (mean 0.88). Table 3 also shows that D_{min} is between 2.21 and 3.12 (mean2.76), while D_{max} ranges from 0.64 to 0.73, with a mean of 0.72.

The multifractal spectrum ($\alpha - f(\alpha)$) is used to further reveal the multifractal characteristics of shale pore structures

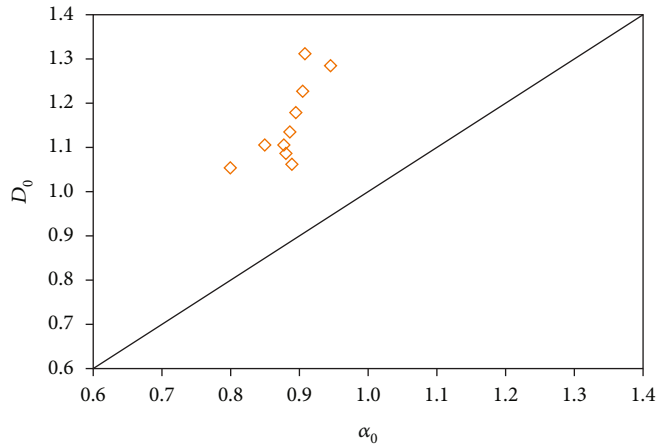

Figure 11: Homogeneity of shale pore structures.

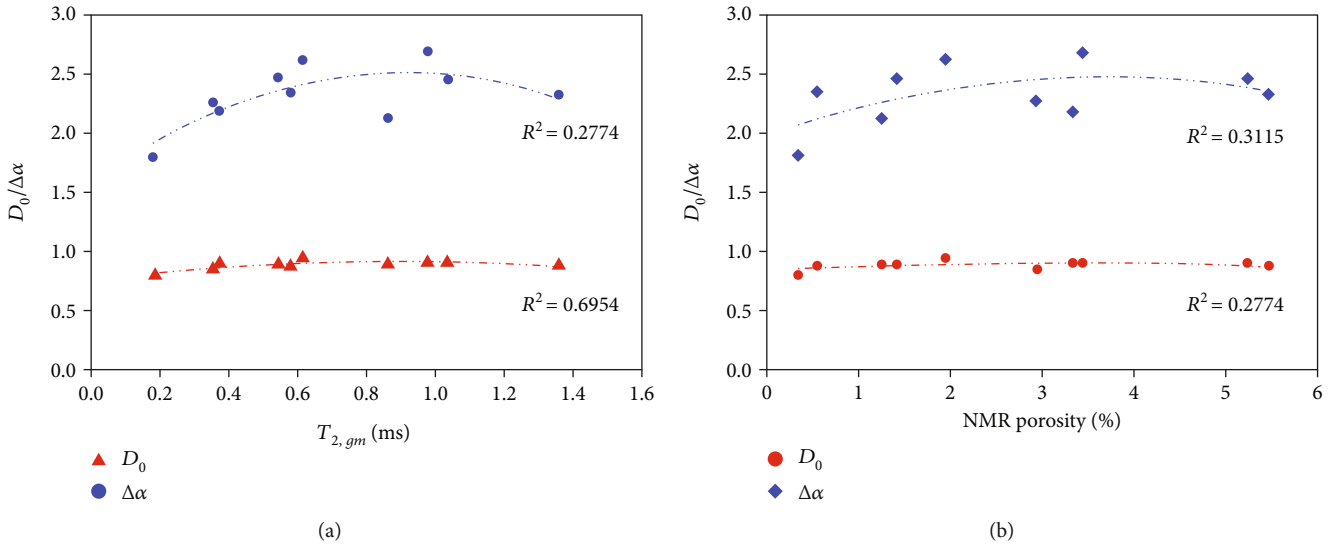

Figure 12: Relationships between pore structure ($T_{2,gm}$ and porosity) and fractal parameters (D_0 and $\Delta\alpha$).

and plotted in Figure 10(b). $f(\alpha)$ increases with increasing α in the left of the crest (corresponding to $q < 0$), while $f(\alpha)$ decreases as α increases, which corresponds to $q > 0$. The singularity strength range ($\Delta\alpha$) represents the widths of the multifractal spectrum, which is another essential multifractal parameter defined as $\alpha_{max} - \alpha_{min}$. $\Delta\alpha$ ranges from 1.81 to 2.68, with an average of 2.33, indicating that the pore structures of the studied shales are heterogeneous. The asymmetry of singularity spectrum (A) values calculated by $(\alpha_0 - \alpha_{min})/(\alpha_{max} - \alpha_0)$ are all less than 1, suggesting a slight fluctuation. The differences between α_0 and D_o are a measure of pore structure heterogeneity. If the pore structure is homogeneous, the data points of α_0 and D_o fall on the same line. However, as shown in Figure 11, α_0 and D_o are deviated from the same line, meaning that the pore structures of shales are heterogeneous and can be better revealed by the multifractal spectra rather than a monofractal model.

To understand the role of pore structures of shale investigated on fractal characteristics, the relationships between the fractal parameters ($D_0$and$\Delta\alpha$) and$T_{2,gm}$and NMR porosity are plotted in Figure 12. The relationships between fractal parameters ($D_0$and$\Delta\alpha$) and$T_{2,gm}$and NMR porosity are all characterized by the parabola curves. The results imply that when the NMR porosity is less than 3.5% and the $T_{2,gm}$ is less than 1.0 ms, as porosity increases, shale pores become larger, leading to the weakness of heterogeneity of shale pore structure. However, when the NMR porosity is larger than 3.5% and the $T_{2,gm}$ is larger 1.0 ms, larger pores result in larger porosity, but the more heterogeneous pore structure.

5. Conclusions

In this paper, the pore structure and multifractal characteristics of Shahezi Formation, Xujiaweizi Fault depression, Songliao Basin, were revealed and the following conclusions were obtained:

The dominant minerals in the continental Shahezi Formation shales are clay minerals, quartz, and feldspar, and the most content of the clay minerals is the illite-smectite. The continental shales are the tight reservoirs with low porosity (mean 1.73%) and the ultralow permeability (mean 0.0707 mD).

The hysteresis loops of ten shales belong to Types H2 and H3. The special surface area ranges from 2.80 m^2/g to 7.30 m^2/g (mean 5.28 m^2/g), and the pore volume is 8.83 – 18.75×10^{-3} cm^3/g (mean 14.15×10^{-3} cm^3/g). The pore size distributions are unimodal, and Type H3 shales have larger pores than Type H2 shales, which may be more conducive to free gas. MICP results indicate that the pore-throat sizes of the studied shales are almost less than 20 nm and show the semimodal distributions.

NMR T_2 spectra at saturated condition (S_o) of ten shale samples show three peeks, *i.e.*, p1 (<1 ms), p2 (1~20 ms), and p3 (>20 ms). The $T_{2,gm}$ values range from 0.18 ms to 1.36 ms, with a mean of 0.69 ms, indicating more nanopores in the continental shales. Moreover, average movable fluid percentage is low, ranging from 1.22% to 15.08% (mean 6.84%).

Multifractal characteristics were analyzed for ten selected shale samples. When $q < 0$, D_q decreases rapidly with q increasing, while D_q decreases slightly as q increases when $q > 0$, indicating that all samples have multifractal nature. The singularity strength range ($\Delta\alpha$) suggests that the pore structures of the studied shales are heterogeneous. The heterogeneity and complexity of continental shale pore structures can be better revealed by the multifractal spectra rather than a monofractal model.

Data Availability

The data applied in this paper has been added to the manuscript.

Conflicts of Interest

The authors declare that they have no conflicts of interest.

Acknowledgments

This work was financially supported by the Natural Science Foundation of Shandong Province (ZR2020QD036).

References

[1] J. B. Curtis, "Fractured shale-gas systems," *AAPG Bulletin.*, vol. 86, pp. 1921–1938, 2002.

[2] G. C. Wang, Y. W. Ju, and K. Han, "Early Paleozoic shale properties and gas potential evaluation in Xiuwu Basin, western Lower Yangtze Platform," *Journal of Natural Gas Science and Engineering*, vol. 22, pp. 489–497, 2015.

[3] J. G. Hu, S. H. Tang, and S. H. Zhang, "Investigation of pore structure and fractal characteristics of the Lower Silurian Longmaxi shales in western Hunan and Hubei Provinces in China," *Journal of Natural Gas Science and Engineering*, vol. 28, pp. 522–535, 2016.

[4] X. Y. Men, S. Tao, Z. X. Liu, W. G. Tian, and S. D. Chen, "Experimental study on gas mass transfer process in a heterogeneous coal reservoir," *Fuel Processing Technology*, vol. 216, article 106779, 2021.

[5] G. C. Wang and Y. W. Ju, "Organic shale micropore and mesopore structure characterization by ultra-low pressure N_2 physisorption: experimental procedure and interpretation model," *Journal of Natural Gas Science and Engineering*, vol. 27, pp. 452–465, 2015.

[6] S. Tao, S. D. Chen, D. Z. Tang, X. Zhao, H. Xu, and S. Li, "Material composition, pore structure and adsorption capacity of low-rank coals around the first coalification jump: a case of eastern Junggar Basin, China," *Fuel*, vol. 211, pp. 804–815, 2018.

[7] W. B. Li, S. F. Lu, J. Q. Li et al., "Geochemical modeling of carbon isotope fractionation during methane transport in tight sedimentary rocks," *Chemical Geology*, vol. 566, article 120033, 2021.

[8] C. N. Zou, D. Z. Dong, S. J. Wang et al., "Geological characteristics and resource potential of shale gas in China," *Petroleum Exploration and Development*, vol. 37, no. 6, pp. 641–653, 2010.

[9] J. C. Cai, W. Wei, X. G. Hu, and D. A. Wood, "Electrical conductivity models in saturated porous media: a review," *Earth-Science Reviews*, vol. 171, pp. 419–433, 2017.

[10] P. F. Zhang, S. F. Lu, J. Q. Li, C. Chen, H. T. Xue, and J. Zhang, "Petrophysical characterization of oil-bearing shales by low-field nuclear magnetic resonance (NMR)," *Marine and Petroleum Geology*, vol. 89, pp. 775–785, 2018.

[11] S. F. Lu, J. Q. Li, P. F. Zhang et al., "Classification of microscopic pore-throats and the grading evaluation on shale oil reservoirs," *Petroleum Exploration and Development*, vol. 45, no. 3, pp. 452–460, 2018.

[12] P. F. Zhang, S. F. Lu, J. Q. Li, and X. C. Chang, "1D and 2D nuclear magnetic resonance (NMR) relaxation behaviors of protons in clay, kerogen and oil-bearing shale rocks," *Marine and Petroleum Geology*, vol. 114, article 104210, 2020.

[13] W. B. Li, S. F. Lu, J. Q. Li et al., "Carbon isotope fractionation during shale gas transport: mechanism, characterization and significance," *Science China Earth Sciences*, vol. 63, no. 5, pp. 674–689, 2020.

[14] C. R. Clarkson, N. Solano, R. M. Bustin et al., "Characterization of tight gas reservoir pore structure using USANS/SANS and gas adsorption analysis," *Fuel*, vol. 103, pp. 606–616, 2013.

[15] P. F. Wang, Z. X. Jiang, W. M. Ji et al., "Heterogeneity of intergranular, intraparticle and organic pores in Longmaxi shale in Sichuan Basin, South China: evidence from SEM digital images and fractal and multifractal geometries," *Marine and Petroleum Geology*, vol. 72, pp. 122–138, 2016.

[16] J. Klaver, G. Desbois, R. Littke, and J. L. Urai, "BIB-SEM characterization of pore space morphology and distribution in postmature to overmature samples from the Haynesville and Bossier Shales," *Marine and Petroleum Geology*, vol. 59, pp. 451–466, 2015.

[17] J. Klaver, G. Desbois, R. Littke, and J. L. Urai, "BIB-SEM pore characterization of mature and post mature Posidonia Shale samples from the Hils area, Germany," *International Journal of Coal Geology*, vol. 158, pp. 78–89, 2016.

[18] Y. Wang, J. Pu, L. H. Wang et al., "Characterization of typical 3D pore networks of Jiulaodong formation shale using nano-transmission X-ray microscopy," *Fuel*, vol. 170, no. 170, pp. 84–91, 2016.

[19] I. G. Torre, J. J. Martín-Sotoca, J. C. Losada, P. López, and A. M. Tarquis, "Scaling properties of binary and greyscale images in the context of X-ray soil tomography," *Geoderma*, vol. 365, article 114205, 2020.

[20] P. F. Zhang, S. F. Lu, J. Q. Li et al., "Broad ion beam-scanning electron microscopy pore microstructure and multifractal characterization of shale oil reservoir: a case sample from Dongying Sag, Bohai Bay Basin, China," *Energy Exploration & Exploitation*, vol. 38, no. 3, pp. 613–628, 2020.

[21] Q. H. Hu, X. Y. Zhang, X. H. Meng, Z. Li, Z. Xie, and M. W. Li, "Characterization of micro-nano pore networks in shale oil reservoirs of Paleogene Shahejie Formation in Dongying Sag of Bohai Bay Basin, East China," *Petroleum Exploration and Development*, vol. 44, no. 5, pp. 720–730, 2017.

[22] P. F. Zhang, S. F. Lu, and J. Q. Li, "Characterization of pore size distributions of shale oil reservoirs: a case study from Dongying sag, Bohai Bay basin, China," *Marine and Petroleum Geology*, vol. 100, pp. 297–308, 2019.

[23] Z. Z. Li, S. F. Lu, X. C. Chang et al., "Micro-pore structure and fractal characteristics of terrestrial shales: a case of Shahezi formation in Xujiaweizi fault depression," *Coal Geology & Exploration*, vol. 49, pp. 151–160, 2021.

[24] X. J. Liu, J. Xiong, and L. X. Liang, "Investigation of pore structure and fractal characteristics of organic-rich Yanchang formation shale in Central China by nitrogen adsorption/desorption analysis," *Journal of Natural Gas Science and Engineering*, vol. 22, pp. 62–72, 2015.

[25] P. F. Zhang, S. F. Lu, J. Q. Li, H. T. Xue, W. H. Li, and P. Zhang, "Characterization of shale pore system: a case study of Paleogene Xin'gouzui Formation in the Jianghan Basin, China," *Marine and Petroleum Geology*, vol. 79, pp. 321–334, 2017.

[26] D. J. Gould and T. J. Vadakkan, "Multifractal and lacunarity analysis of microvascular morphology and remodeling," *Microcirculation*, vol. 18, no. 2, pp. 136–151, 2011.

[27] M. G. Hu, J. F. Wang, and Y. Ge, "Super-resolution reconstruction of remote sensing images using multifractal analysis," *Sensors*, vol. 9, no. 11, pp. 8669–8683, 2009.

[28] S. Q. Guo, D. S. Xiao, S. F. Lu, L. C. Zhang, and M. W. Gu, "Quantificational characterization of tight reservoir pore size distribution of Shahezi Formation in Xujiaweizi Fault Depression," *Journal of Central South University (Science and Technology)*, vol. 47, pp. 3742–3751, 2016.

[29] M. Wang, Y. F. Sun, W. G. Wang, Y. Wang, and L. Shi, "Gas generation characteristics and resource potential of the deep source rock in Xujiaweizi fault depression, northern Songliao Basin," *Nature Gas Geoscience*, vol. 25, pp. 1011–1018, 2015.

[30] D. S. Xiao, S. Jiang, D. Thul, S. F. Lu, L. C. Zhang, and B. Li, "Impacts of clay on pore structure, storage and percolation of tight sandstones from the Songliao Basin, China: implications for genetic classification of tight sandstone reservoirs," *Fuel*, vol. 211, pp. 390–404, 2018.

[31] P. Q. Zhao, Z. L. Wang, Z. C. Sun, J. C. Cai, and L. Wang, "Investigation on the pore structure and multifractal characteristics of tight oil reservoirs using NMR measurements: Permian Lucaogou Formation in Jimusaer Sag, Junggar Basin," *Marine and Petroleum Geology*, vol. 86, pp. 1067–1081, 2017.

[32] T. C. Halsey, M. H. Hensen, L. P. Kadanoff, I. P. Kadanoff, and I. S. Boris, "Fractal measures and their singularities: the characterization of strange sets," *Nuclear Physics B-Proceedings Supplements*, vol. 33, pp. 1141–1151, 1986.

[33] A. Chhabra and R. V. Jensen, "Direct determination of the f(a) singularity spectrum," *Physical Review Letters*, vol. 63, pp. 605–616, 1989.

[34] S. J. Gregg and K. S. W. Sing, *Adsorption Surface Area and Porosity, Second Ed*, Academic Press, New York, 1982.

[35] A. J. Bolton, A. J. Maltman, and Q. Fisher, "Anisotropic permeability and bimodal pore-size distributions of fine-grained marine sediments," *Marine and Petroleum Geology*, vol. 17, no. 6, pp. 657–672, 2000.

[36] Y. B. Yao, D. M. Liu, Y. Che, D. Z. Tang, S. H. Tang, and W. H. Huang, "Petrophysical characterization of coals by low-field nuclear magnetic resonance (NMR)," *Fuel*, vol. 89, no. 7, pp. 1371–1380, 2010.

[37] T. W. Li, H. K. Guo, H. B. Li, Y. Lu, and X. J. Xue, "Research on movable fluids in shale gas reservoirs with NMR technology," *Special oil and gas Reservoirs*, vol. 19, pp. 107–123, 2012.

[38] M. J. Tan, K. Y. Mao, X. D. Song, Y. Xuan, and J. J. Xu, "NMR petrophysical interpretation method of gas shale based on core NMR experiment," *Journal of Petroleum Science and Engineering*, vol. 136, pp. 100–111, 2015.